Temperature-induced electride transition in dense lithium

Yong Wang,[1,*] Junjie Wang,[1,*] Andreas Hermann [2] Shuning Pan,[1] Jiuyang Shi,[1] Hui-Tian Wang,[1]
Dingyu Xing,[1] and Jian Sun [1,†]

[1]*National Laboratory of Solid State Microstructures, School of Physics and Collaborative Innovation Center of Advanced Microstructures,*
Nanjing University, Nanjing 210093, China
[2]*Centre for Science at Extreme Conditions and SUPA, School of Physics and Astronomy, The University of Edinburgh,*
Peter Guthrie Tait Road, Edinburgh EH9 3FD, United Kingdom

As a prototypical light metal, lithium shows various and intriguing behaviors including electride character under high pressure. It has a pronounced melting line depression from 40 to 60 GPa, yet a precise and detailed understanding of this melting minimum remains elusive. Here, using computations that include metadynamics, crystal structure searching, and molecular dynamics with machine learned potentials, we demonstrate a temperature-induced electride (pocketlike to tubelike) transition accompanied by complex structural phase transitions in dense premelting lithium. The possible rearrangement of nearest neighbors from three-coordinated net to dimers and the premelting collective atomic motion affected by this electronic transition demonstrates the combined influence of temperature and electronic structure on the high-pressure behaviors of metals.

I. INTRODUCTION

The pioneering predictions by Neaton and Ashcroft [1] on the pairing in dense lithium became a symbol for the complex structural and electronic changes under pressure. Studies showed that the ground-state structure of lithium at zero pressure is inconsistent with the previously assumed 9R phase, and proved it should be fcc [2–4]. High-pressure experiments have investigated a series of solid phase transitions in Li at low temperature [5–8]: bcc (zero pressure 300 K) $\xrightarrow{\sim 7 \text{ GPa}}$ fcc $\xrightarrow{\sim 39 \text{ GPa}}$ $hR1$ $\xrightarrow{\sim 42 \text{ GPa}}$ $cI16$ $\xrightarrow{\sim 60 \text{ GPa}}$ $oC88$ $\xrightarrow{\sim 70 \text{ GPa}}$ $oC40$ $\xrightarrow{\sim 95 \text{ GPa}}$ $oC24$. With these transformations, dense lithium exhibits unusual behaviors including superconductivity [9–11], electronic transitions [12,13], and the existence of a melting maximum and subsequent minimum [14–18]. From calculations, low symmetry and electride phases (where electrons localize in interstitial sites) have been also proposed for dense lithium [19–23].

Specifically, the melting of lithium reaches a maximum of 520 K at ~ 8 GPa and drops to a minimum at around 50 GPa. Experimentally, this minimum was observed to be around 190 K between 40 and 60 GPa in Ref. [8], but assigned at 306 K and 44 GPa in Ref. [15]. This discrepancy was reinvestigated recently, and the melting was found to be close to room temperature between 40 and 60 GPa. Besides, an unresolved solid phase was proposed in this pressure range at 250–300 K [18].

In first principles calculations, the melting of lithium, without considering nuclear quantum effects (NQEs), occurs around 250–300 K at 65 GPa [16] and 270 K at 50 GPa [17].

Considering the NQEs using *ab initio* path-integral molecular dynamics (PIMD), it is found to be 275 K at 45 GPa [24]. These results are close to the experimental values in Refs. [15,18]. Another computational study [25] that used the Wigner-Kirkwood approximation for NQEs in the liquid and the lattice entropy in the solid phase obtained melting around 200 K between 40 and 60 GPa, which seems to be similar to Ref. [8].

While many previous studies focus on the melting curve or the liquid-liquid phase transition (LLPT) in dense lithium [16,17,24,25], its solid potential energy surface (PES) at finite temperature remains elusive. Here, we employed extensive theoretical methods [26–31] including machine learning assisted crystal structure searching, metadynamics, path integral schemes, and finite-temperature phonon calculations to explore the undetermined finite-temperature phases of lithium and to provide details of transformation mechanisms. We find several structures of lithium at 50 GPa energetically competitive to the known $cI16$ phase. As the temperature increases, our metadynamics and *ab initio* molecular dynamics (AIMDs) show that the fully localized electride with electrons in individual pockets in the low temperature $cI16$ partially delocalizes into a tubelike electride through complex structural transformations accompanied by a possible dimerization of lithium atoms. In addition, a melting point of at least 300 K and a premelting regime with collective atomic motion in lithium are identified.

II. METHODOLOGY

Density functional theory (DFT) calculations, including structure optimizations, electronic structures, and AIMD simulations, in this study are performed using the Vienna *ab initio* simulation (VASP) code [32], together with the PAW [33]

---

*These authors contributed equally to this work.
†Corresponding author: jiansun@nju.edu.cn

potentials and the Perdew-Burke-Ernzerhof (PBE) exchange-correlation functional [34]. An all-electron $1s^2 2p^1$ valence space, a 650-eV energy cutoff for the plane wave basis set, and a k-point sampling grid spacing of $0.05 \times 2\Pi$ Å^{-1} for the Brillouin zones of all cells were used for static optimizations and electronic properties calculations. Since for the large supercell (432 atoms) for metadynamics and AIMDs it was not feasible to use the all-electron potential, a $2p^1$ valence space and 250-eV plane wave energy cutoff were used for those calculations instead. Necessary comparisons between these two PAW data sets at 50 GPa were made in Appendix C and showed that this did not change the conclusions.

The *ab initio* metadynamics simulations were carried out at 0 and 280 K with a simulation supercell consisting of 432 atoms with a Γ-centered k-point sampling. The unit cell parameters were used as the collective variables. The system was first equilibrated at the given temperature and pressure. The Hessian matrix required for metadynamics was then constructed by geometry optimization at 0 K by using finite differences of the stress tensor followed by diagonalization. For the bias potential, a Gaussian width and height of 15 (kbar Å^3)$^{1/2}$ and 225 kbar Å^3 were used, respectively. For 0 K, direct relaxation and optimization of the internal atomic coordinates were performed; for 280 K, each metastep consisted of 500 NVT AIMD steps with a total simulation time of 0.5 ps using a Nosé-Hoover thermostat [35,36]. Structures obtained in selected metasteps were quenched to 0 K for identification of their crystal structures.

AIMD was performed using the isothermal-isobaric (NPT) ensemble with a Parrinello-Rahman barostat [37] and a Langevin thermostat [38], as well as the canonical (NVT) ensemble with a Nosé-Hoover thermostat [35,36], as implemented in the VASP code, employing a time step of 1 fs. A 432-atom supercell of $cI16$ and a 448-atom supercell of $C2/m$ were used. The Brillouin zone was sampled at the Γ point. Simulations ran for at least 15 ps, and some of the trajectories were extended up to 50 ps to check their stability. The initial 5 ps were used for thermalization and the last 10 ps were used to extract the statistical quantities. Molecular dynamics (MD) with the machine learning potential was performed using LAMMPS [39] with periodic boundary conditions and a time step of 1 fs.

The structure search is based on our in-house code machine learning and graph theory assisted universal structure searcher (MAGUS) [26,40], which uses machine learning potentials to accelerate local optimization and graph theory to reduce the conformational space. This method has been successfully applied in many systems including planetary materials [41–44]. The MLIP [29] package was used to train a machine learning potential to do structure relaxations and molecular simulations to reduce the expensive first-principle calculations. The potential is initially trained on DFT single point energy calculation results of some random structures since it has been proven that starting with a pretrained potential can decrease the number of DFT calculations compared to starting from scratch [45]. Extrapolative or badly fitted configurations are selected and added to the train set to actively improve the potential during the search process. In this study, the RMSEs of the potential are 10.4 meV/atom for the energies, 60.2 meV/Å for the forces, and 0.94 GPa for the stresses.

The path-integral MD (PIMD) simulations are performed with the *i*-PI wrapper for the nuclear degrees of freedom [31], with interatomic forces determined by DFT calculations using the VASP code, in the isothermal-isobaric (NPT) ensemble. A generalized Langevin equation thermostat [46] was attached for PIMDs, which ensures the convergence with eight beads.

Lattice dynamics calculations were performed using the PHONOPY package [47]. Renormalized phonon spectra including anharmonicity and temperature dependent phonon properties were calculated using the DYNAPHOPY package [30]. The velocity-autocorrelation functions from AIMD were projected onto the harmonic displacement vectors that were determined in the phonon calculations. The finite-temperature phonon dispersions were then obtained by calculating renormalized force constants that correspond to the quasiparticle phonon frequencies at the high symmetry points, which provided an updated dynamical matrix that was then interpolated in the **q** space, akin to lattice dynamics calculations. From the resulting set of phonon frequencies $\omega(q, v)$ the partition function Z can be written as

$$Z = \exp\left(-\frac{\varphi}{k_B T}\right) \prod_{qv} \frac{\exp\left(-\frac{\hbar\omega(qv)}{2k_B T}\right)}{1 - \exp\left(-\frac{\hbar\omega(qv)}{k_B T}\right)}.$$

Phonon free energies F were calculated as

$$F = -k_B T \ln Z$$
$$= \varphi + \frac{1}{2}\sum_{qv} \hbar\omega(qv) + k_B T \sum_{qv} \ln\left[1 - \exp\left(-\frac{\hbar\omega(qv)}{k_B T}\right)\right],$$

where φ is the total energy. Phonon entropies S can be obtained as

$$S = -\frac{\partial F}{\partial T} = \frac{1}{2T}\sum_{qv} \hbar\omega(qv)\coth[\hbar\omega(qv)/2k_B T]$$
$$- k_B \sum_{qv} \ln\{2\sinh[\hbar\omega(qv)/2k_B T]\}.$$

III. RESULTS

A. Crystal structures

Potential lithium crystal structures at 50 GPa with up to 40 atoms per unit cell have been searched for using MAGUS at 0 K. Several energetically competitive candidates were found with enthalpy differences less than 5 meV/atom, such as the known I-$43d$ ($cI16$) phase, as well as a monoclinic $C2/m$ phase (eight atoms per unit cell), and a Pa-3 phase (28 atoms per unit cell). Subsequent *ab initio* metadynamics also confirmed complex structural phase transitions.

Ab initio metadynamics calculations starting from the $cI16$ phase at 53 GPa were carried out to study lithium's finite-temperature free energy landscape. Considering that the high temperature structures of sodium around its melting line minimum have complex unit cells with hundreds of atoms [48], a $3\times3\times3$ supercell with 432 Li atoms was used. However, we may still miss some competitive phases with the comparatively larger unit cell. Transformation details of the structure during 280-K metadynamics show the rearrangements of Li atoms [Fig. 1(a)]. Looking down the c axis, the zigzag atomic chains in $cI16$ along the a and b
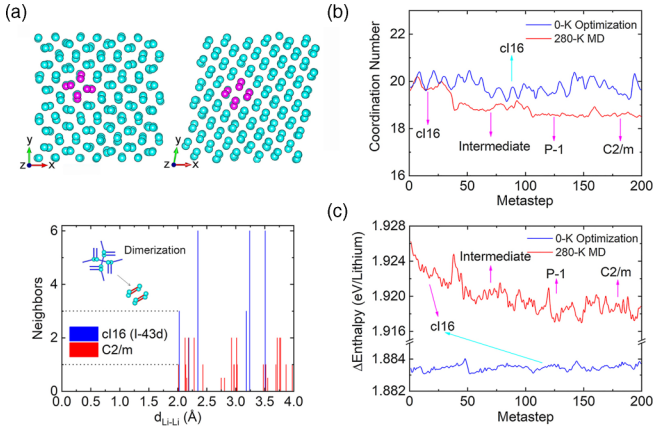
FIG. 1. The finite-temperature structural transformations in dense lithium at 53 GPa. (a) Details of atomic environment change (top) during 280-K metadynamics seen along the c axis. Histogram (bottom) of Li-Li coordination separations shows the smallest transformation unit (marked as purple in supercells) dimerized between metastep 2 and metastep 195. (b) Evolution of coordination number during metadynamics simulations starting from $cI16$ at 0 and 280 K. (c) Evolution of enthalpy change in metadynamics at 0 and 280 K. Different potential energy surfaces emerge at different temperatures.

directions all align parallel along the a axis. The changes within the eight-atom unit of $cI16$ (highlighted in purple) demonstrate that nearest neighbor environments evolve from threefold coordinated nets into Li-Li dimers, which can also be directly determined through the Li-Li coordinations for $cI16$ and $C2/m$ [Fig. 1(a)]. Interestingly, the pressure-induced dimerization was predicted by Neaton and Ashcroft [1] in the $Cmca$-16 structure above 100 GPa. This structure was later superseded by more stable high-pressure phases [8], but

our results indicate that finite temperature may induce this kind of dimerized state in lithium, and also effectively reduce the dimerization pressure to around 50 GPa. The evolution of the atomic coordination number [measured with uniform cutoff radius 3.514 Å, Fig. 1(b)] reveals a series of complex structural transformations at 280 K and also confirms that this path is blocked at low temperature. Average structures extracted from metadynamics at different stages are further relaxed using 280-K AIMDs and then optimized to access some crystal candidates. Between 50 and 100 metasteps, the system exhibited intermediate properties where no good structural candidate was found. After 100 metasteps, we found two possible candidate structures (space groups P-1 and $C2/m$), which both feature Li dimerization. The $C2/m$ phase is similar to the structure we found using crystal structure searching. Meanwhile, unlike phase transitions that occur at low temperature [49–51] the enthalpy differences between phases we identified is not remarkable [Fig. 1(c)]. Despite this, enthalpy evolution at 0 and 280 K still show that high temperature reshapes the free energy landscape and that small enthalpy differences between competitive states may induce the structural diversity in high-temperature dense lithium, just like in sodium [48] and this diversity might explain the discrepancies between prior experiments [8,15,18]. More results of crystal structure searching and metadynamics can be found in Table I.

B. X-ray diffraction patterns

The x-ray diffraction (XRD) peaks of the recent experiments [18] at 40–60 GPa and 250–275 K are not compatible with $cI16$. In addition, the scattering of x rays from the very small dense lithium samples is extremely weak, and the experimental data are not sufficient to unambiguously assign structures. We compared experimental XRD with the simulated

TABLE I. Structural parameters of competitive structures including the known $cI16$ of dense lithium at 53 GPa which are found by crystal structure searching and finite-temperature simulations. The differences of enthalpy between them are less than 10 meV/atom.

| Space group	Number of atoms	Lattice parameter (Å)	Lattice angle (deg)	Atomic coordinates (fractional)
$C2/m$	8	$a = 7.9317$	$\alpha = 90$	(0.031 28, 0.5, 0.315 37)
		$b = 2.1291$	$\beta = 128.58$	(0. 282 99, 0.5, 0.813 69)
		$c = 5.0002$	$\gamma = 90$	
Pa-3	28	$a = 6.11$	$\alpha = \beta$	(0.195 67, 0.435 85, 0.841 00)
			$= \gamma = 90$	(0, 0, 0)
I-$43d$ ($cI16$)	16	$a = 5.0601$	$\alpha = \beta$	(0.809 28, 0.809 28, 0.809 28)
			$= \gamma = 90$	
P-1	4	$a = 4.0376$	$\alpha = 76.43$	(0.752 85, 0.141 85, 0.936 12)
		$b = 4.2029$	$\beta = 73.05$	(0.746 91, 0.816 88, 0.441 21)
		$c = 4.1616$	$\gamma = 80.16$	(0.252 97, 0.357 21, 0. 058 59)
				(0.753 35, 0.317 67, 0.437 16)
P-1	6	$a = 2.0657$	$\alpha = 78.21$	(1.743 88, -0.745 02, −0.710 14)
		$b = 4.0980$	$\beta = 95.74$	(1.482 03, −0.753 45, −0.376 03)
		$c = 6.1567$	$\gamma = 75.85$	(1.610 62, −0.751 48, −0.041 51)
$C2/c$	4	$a = 2.5071$	$\alpha = 90$	(0.031 28, 0.5, 0.315 37)
		$b = 3.4052$	$\beta = 134.17$	(1.000 00, −0.124 40, 0.750 00)
		$c = 5.3537$	$\gamma = 90$	
P-1 (from metadynamics)	4	$a = 2.1247$	$\alpha = 72.41$	(0.211 24, 0.253 69, 0.306 53)
		$b = 4.0836$	$\beta = 75.91$	(−0.477 10, 0.753 94, 0.191 68)
		$c = 4.1533$	$\gamma = 75.16$	
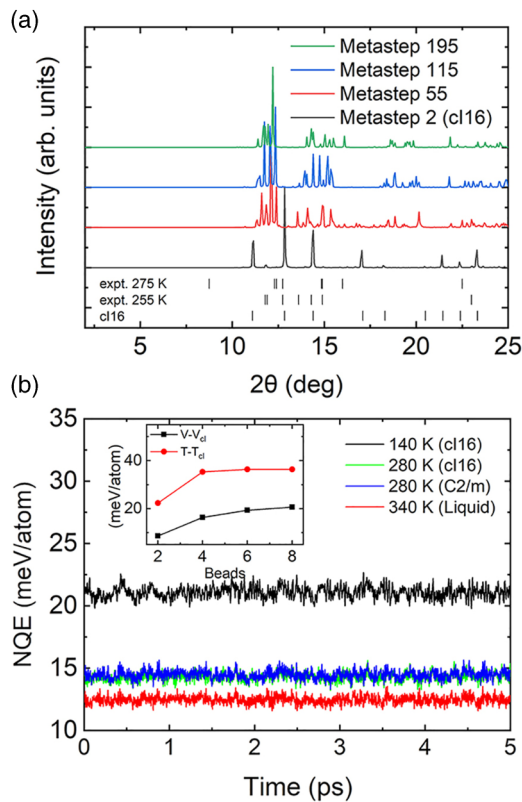
FIG. 2. (a) Simulated XRD patterns based on structures extracted from 280-K metadynamics. Black ticks are experimental peak positions from Ref. [18]. (b) Centroid-virial nuclear quantum effects in lithium at 53 GPa and different temperatures. NQEs of different structures at the same T is barely different. Inset shows the per-atom quantum contribution to the potential energy and quantum kinetic energy converged with eight PI beads compared to classical AIMD.

XRD pattern based on the structures extracted from our metadynamics simulations [Fig. 2(a)]. The changes to the patterns from $cI16$ to the new structures caused by structural transformations is consistent with the experimental data, inasmuch as the peaks of the new structures have moved to higher 2θ compared to $cI16$, with dominant features around $2\theta = 12°$ and $15°$. Although not all the peaks fit to the experimental data perfectly, considering that our study may explore a finite part of the free energy surface and the uncertainties resulting from challenges in experiments, the overall agreement between our results and the recent experimental data [18] is still somehow reasonable.

C. Nuclear quantum effects and phonon entropy

Since the $C2/m$ phase was not only found in our crystal searching as the second lowest enthalpy structure (the lowest one is $cI16$) but was also identified in metadynamics, we used it as the most promising candidate phase to calculate free energies to trace potential finite temperature phase transitions. The time-averaged enthalpy of $cI16$ at 240 K and 53 GPa is still about 2.51 meV/atom lower than $C2/m$ in AIMD simulations. Since the lithium atom is light, nuclear quantum effects (NQEs) may play an important role in the phase transformations of lithium. Therefore, we study the NQEs by involving
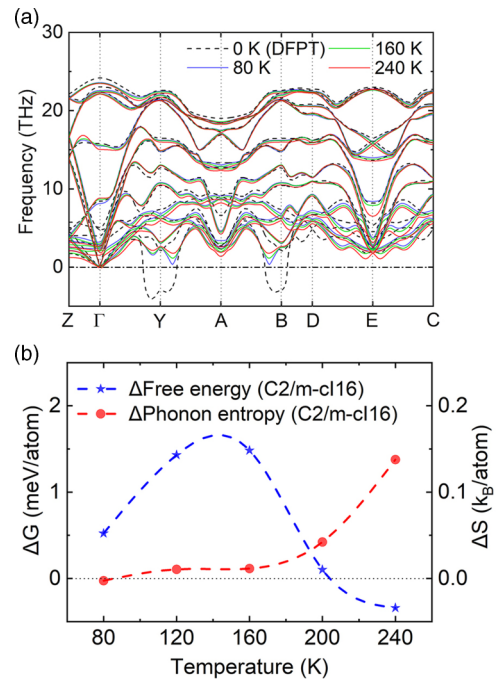

FIG. 3. (a) Phonon dispersion curves of $C2/m$ as a function of temperature at 53 GPa. The softening induced at low temperature is gradually suppressed (see high symmetry points Y, B). (b) Free energy and phonon entropy difference between $cI16$ and $C2/m$ as function of temperature.

the path integral molecular dynamics (PIMD) methods [31]. By applying this scheme, eight-bead PIMD simulations of $cI16$ at 53 GPa and 250 K gave converged results. Our results for the NQEs in lithium are in the same range as those from PIMD simulations using the Andersen thermostat in Ref. [24]. However, different temperatures influence NQEs much more than different structures [Fig. 2(b)]: for $cI16$ and $C2/m$ near melting at 280 K, the difference between their NQEs is only 0.15 meV/atom, which is negligible.

Furthermore, to address the free energy difference, entropy must be considered. For the solid crystal, the atomic entropy mainly comes from the thermal vibrations, otherwise known as phonon entropy. A typical example reported for phase transitions driven by entropy is that the bcc iron phase may be more stable than the hcp phase at Earth's inner core conditions [52]. The harmonic phonon spectra of $C2/m$ shows similar instabilities to bcc iron. To confirm whether it is stable at finite temperature, we calculated the finite-temperature phonon dispersions of $C2/m$ that include lattice anharmonicity through extracting phonon quasiparticles from MD simulations [30]. The phonon softening of $C2/m$ induced by anharmonicity is gradually suppressed, which means this phase could be stabilized by temperature [Fig. 3(a)]. The phonon entropy and resulting Gibbs free energies of $C2/m$ and $cI16$ calculated from finite-temperature spectra change with temperature and might compensate for their enthalpy difference. For instance, at 240 K, $C2/m$ has a smaller Gibbs free energy (0.34 meV/atom), due to a difference of phonon entropy between $cI16$ and $C2/m$ of about $0.138 k_B$/atom [Fig. 3(b)]. If the diffusion entropy of collective atomic motion in $C2/m$ is
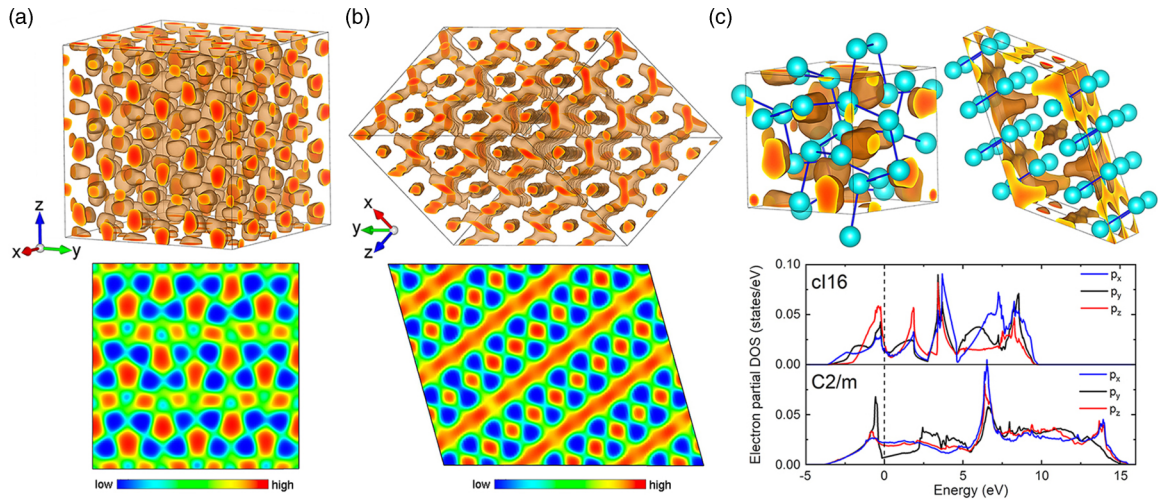
FIG. 4. Electride transition during the finite-temperature structural transformations in dense lithium at 53 GPa. (a), (b) Evolution of electron localization from metastep 2 (initial $cI16$) in (a) to metastep 195 in (b). Top panels show electron localization functions (ELFs) isosurfaces ELF = 0.75. Bottom panels show two-dimensional cross sections that confirm the electride transition from full to partial localization during 280-K metadynamics. (c) ELF = 0.75 isosurfaces of $cI16$ (top left) and monoclinic structure $C2/m$ (top right). Blue solid lines connect the nearest neighbors. Bottom graph shows electronic projected density of states for $cI16$ and $C2/m$. The closure of the pseudogap in two directions (p_x and p_z) in $C2/m$ reflects the electride transformation.

considered (see below), the free energy of $C2/m$ might reduce further. These free energy calculations reflect that in dense lithium the free energy differences between the competitive phases near melting could be very small (akin to a complex free energy surface with small basins of similar depths).

D. Temperature-induced electride transition

Previous studies revealed the localization of electrons in interstitial sites (the so-called electride character) in dense lithium [1,19–23]. However, little is known about the influence of temperature on electrides. We performed analyses of electronic structure changes during the metadynamics to identify the intrinsic electronic drive behind the structural transition. At 280 K, the full electron localization (pocketlike) at metastep 2, typical for the initial $cI16$ phase [Fig. 4(a)], gradually evolves into a partial tubelike localization. We plotted one representative snapshot of these electride tubes at metastep 195 in Fig. 4(b). To investigate this electronic transformation clearly, the electronic characteristics of $C2/m$, in real and reciprocal space, are compared to $cI16$ in Fig. 4(c). The electride character of three-coordinated lithium atoms in $cI16$ can be seen in the electron localization function (ELF = 0.75) plots, which suggests full localization of electrons that form pseudoanions in the interstitial space. However, in the finite-temperature monoclinic $C2/m$ structure, the electron localization is partially lifted and becomes a tubelike localization. This implies that temperature might reconstruct high-pressure electrides, which aligns with complex liquid behavior induced by electrides in high pressure-temperature metals, such as the tetrahedral clustering in melted lithium [16] and electride crossover in liquid potassium [53].

This electride transition is also reflected by the projected electronic density of states (PDOS) [Fig. 4(c)]. For the $cI16$ structure, there are pseudogaps near the Fermi level in all

the p_x, p_y, and p_z orbitals. In the high-temperature $C2/m$ structure, two of the pseudogaps are flattened and only one pseudogap remains, along the localized p_y orbital, again suggesting much reduced electron localization in the $C2/m$ structure.

E. Premelting atomic collective motion

AIMD simulations using the NPT ensemble at 50 GPa from 180 to 360 K were performed to determine the melting point of dense Li in this anomalous pressure range. Since the influence of NQEs at finite temperature is negligible, we used classical nuclei AIMD. The "heat until melting" method was applied in a 432-atom $cI16$ supercell. Analyses of mean square displacements (MSDs) extracted from the last 10 ps of equilibrated trajectories of dense lithium put the melting point between 300 and 360 K [Fig. 5(a)]. We notice small steps in MSDs at and above 260 K that signify a finite-temperature structural reorganization of $cI16$. Even at 360 K, full melting (divergent MSD) happens after this step change. This change also corresponds to a temperature-induced electride transition: Appendix B shows that the premelting structure has the same tubelike electride character as found in the metadynamics simulations. We have also tested the melting point with the NVT ensemble and the same melting temperature range was found. However, $cI16$ did not undergo a structural reorganization until full melting in NVT simulations, which indicates that the P-T path may also affect the final results and alleviate the discrepancy of previous different results [8,14–18,24,25]. Considering the complex finite-temperature free energy surface, maybe more enhanced sampling methods can be used to study the finite-temperature phase transitions. The pair correlation functions $g(r)$ at relevant temperatures are plotted in Fig. 5(b). The disappearance of the next nearest neighbor peak for $T \geqslant 260$ K can be connected to changes
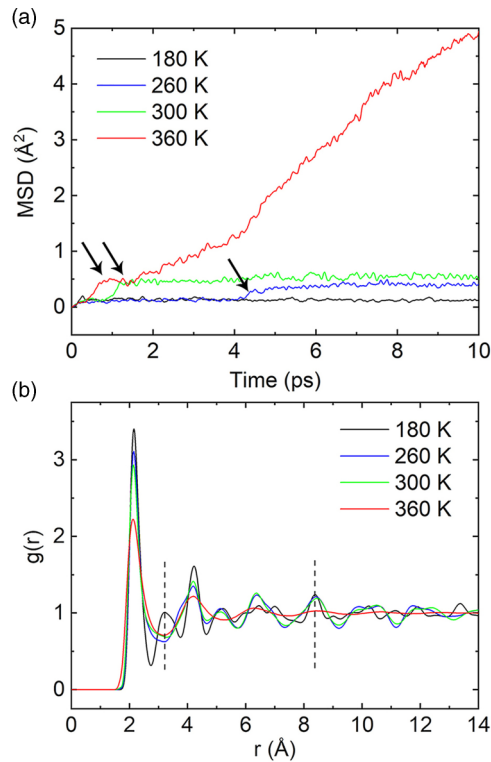
FIG. 5. Determination of melting point at melting minimum pressure range (50 GPa) and premelting regime induced by electride transition. (a), (b) Mean squared displacements (MSDs) and pair correlation functions $g(r)$ extracted from AIMD trajectories at 50 GPa. All MD simulations start from initial $cI16$. Small step changes (marked by black arrows) in MSDs at $T \geqslant 260$ K confirm the structural transformation with the electride transition near melting. Vertical black dashed lines in $g(r)$ highlight the prominent changes.

to the local structure in the monoclinic transition while the structure maintains long range order compared to full liquid.

To investigate the influence of the electron redistribution during melting, we extended one trajectory at 300 K to 50 ps. We observed collective atomic motion along the tubelike electride chain below the melting temperature, triggered by the formation of Frenkel-like defects on fs time scales (Fig. 6). This behavior has been seen in several metallic systems [54–56] and has a close connection to the electride structure [57,58]. We can link our observations to the Vicsek model [59], a simple and general model to interpret the collective behavior of active matter. The Vicsek model's rule of aligning the direction of motion of particles corresponds to the presence of the electride tube that tends to align atomic motion along a specific direction, while the level of random perturbations applied to particle motion in the model is analogous to the temperature in our situation. The kinetic phase transition in the model with spontaneous collective motion corresponds to the premelting phenomenon seen here. From this point of view, we can extend the concept of collective motion to include the premelting behaviors in metals under high pressure. Meanwhile, this behavior may provide sufficient entropy to stabilize the partially molten state as in other systems [56,57].
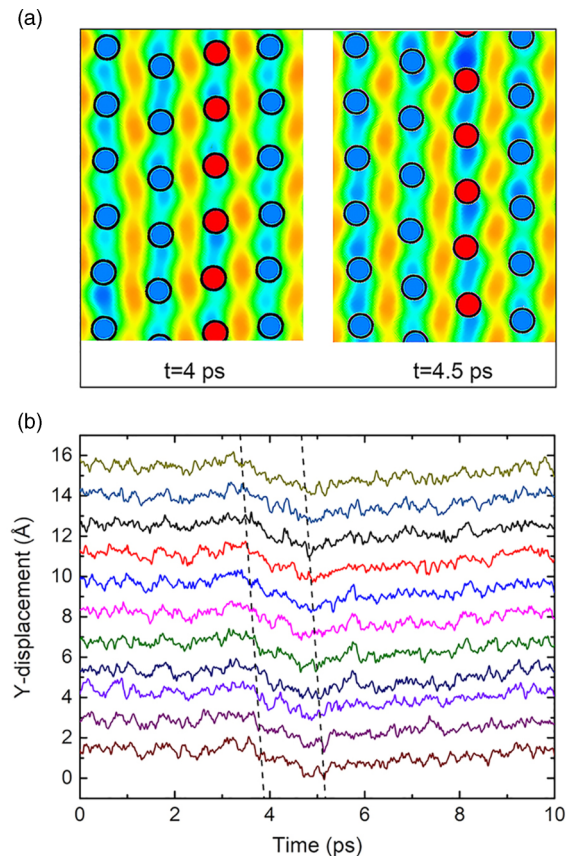

FIG. 6. (a) Snapshots of initial and final positions of atoms during the collective atomic motion at premelting regime (300 K), together with their tubelike ELF environments (blue/red circles represent static/moving atoms, ELF color scheme as in Fig. 4). (b) Specific changes of atoms' displacements over time during collective motion along the tubelike electride direction. Each colored line represents the Y coordinate of a single atom along collective motion, slanted dotted lines are guide to the eye for the time sequence of atomic motions triggered as the first atom leaves the equilibrium position and induces neighbors' motion.

IV. CONCLUSIONS

In summary, we observed a temperature-induced electride transition from fully localized pocketlike electride to partially localized tubelike electride in dense lithium accompanying several finite-temperature candidate phases for lithium's undetermined solid phase near the melting minimum. This can be seen as an evolution of electronic structure from three-dimensional localization induced by high pressure to the partially free electron behavior following temperature-induced structural changes. A dimerization of lithium might occur at around 50 GPa, which is a much lower pressure than proposed by Neaton and Ashcroft [1] previously (> 100 GPa). The melting is affected by the anisotropy of the electronic structure. Collective atomic motion prior to melting along the direction of the electride tubes might lead to extra entropy gain and less potential energy increase. Our observations may also be connected to Vicsek model's collective motion state in active matter, where the tendency of atoms to move along the direction of the electride and the temperature
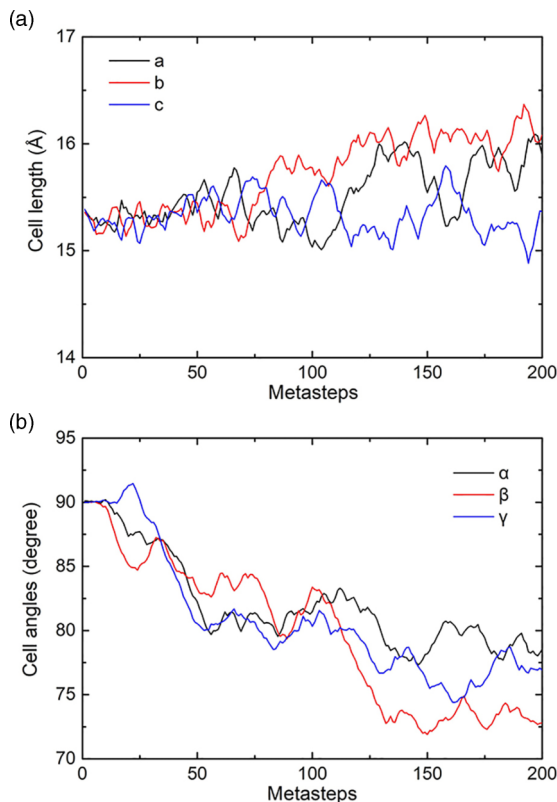
(a)

(b)

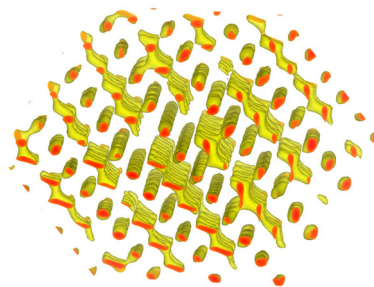FIG. 7. Evolution of cell edges length (a) and cell angles (b) during 280-K metadynamics run.

FIG. 9. Electron localization function isosurface (ELF = 0.8) extracted from *NPT* AIMD simulations near melting 300 K, with atoms and cell omitted for clarity.

APPENDIX A: QUANTITIES EVOLVED DURING METADYNAMICS SIMULATIONS

Figure 7 gives a detailed overview of how the lattice parameters, the collective variables during the metadynamics simulations, changed during the 280-K run. The starting configuration is the low temperature structure *cI*16 at 53 GPa. The changes in the lattice vectors' lengths and cell angles confirm the existence of complex phase transitions in the premelting regime in dense lithium.

Figure 8 compares the phonon DOS's of structures quenched from the metadynamics at steps 2 and 195, respectively. The changes in the mid- and high-frequency range would increase phonon entropy of the final structure com-
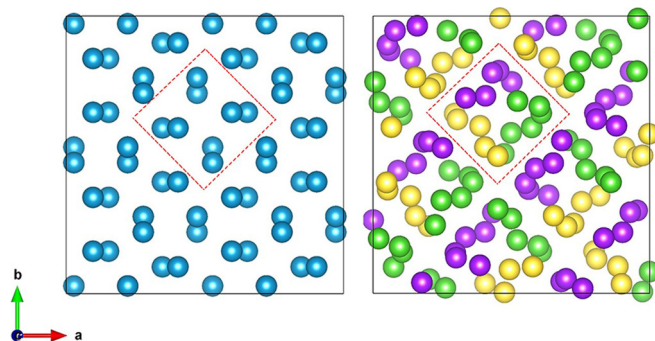
correspond to the update condition and random perturbation, respectively. We also found that nuclear quantum effects seem to be quite small in this system and much more sensitive to temperature rather than structure. These abundant and interesting phenomena demonstrate that electrons play an important role in finite-temperature phase transitions and premelting anomalies. To describe such intriguing scenarios for premelting, multidisciplinary ideas beyond the classical Lindemann criterion may be required.
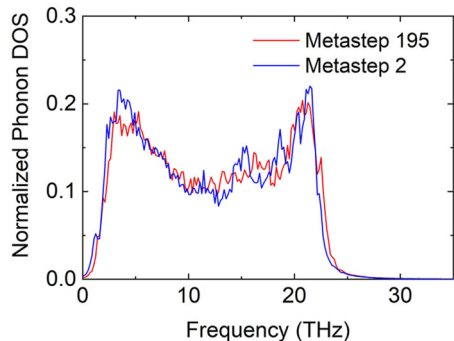
FIG. 8. Vibrational spectra (phonon DOS) calculated from structures from different steps of metadynamics at 53 GPa 280 K.

FIG. 10. The known low-temperature *cI*16 structure (left) and unstable new structure in 280-K AIMDs using small-size (128-atom) supercell viewed along *c* axis.

TABLE II. Diffusion coefficients (D) calculated from 53-GPa AIMDs at different temperatures using two methods [mean square displacement (MSD) and velocity autocorrelation function (VACF)].

Temperature (K)	D_{MSD} (m^2/s)	D_{VACF} (m^2/s)	State
140	1.126×10^{-12}	6.137×10^{-12}	solid
180	1.153×10^{-12}	5.752×10^{-12}	solid
220	2.371×10^{-11}	1.304×10^{-11}	solid (electride transition occurs)
260	3.839×10^{-11}	2.145×10^{-11}	solid
300	4.167×10^{-11}	2.971×10^{-11}	solid
340	4.267×10^{-11}	4.922×10^{-11}	solid
360	2.861×10^{-9}	0.971×10^{-9}	solid $\rightarrow$ liquid
400	3.502×10^{-9}	1.156×10^{-9}	liquid

pared to initial $cI16$. The phonon entropy based on phonon DOS can be calculated by integrating the product of DOS and phonon entropy quantum weighting functions $W_S^Q(v) = \frac{\beta h v}{\exp(\beta h v) - 1} - \ln[1 - \exp(-\beta h v)]$ along the frequency domain.

APPENDIX B: QUANTITIES EXTRACTED FROM NPT MELTING SIMULATIONS

Figure 9 provides the electronic structure of lithium in the premelting regime during AIMD simulations. The characteristic tubelike electride character confirms the temperature-induced electride transition seen in the metadynamics simulations.

Figure 10 illustrates how finite size effects can lead to unstable structures in the MD. Using a 128-atom supercell, the unit cell in $cI16$ (marked by a red square in Fig. 10) with zigzag chains transformed to three twisted chains (marked as different colors in Fig. 10). This new structure with helical chains cannot be assigned to an explicit space group and is unstable (i.e., disappears) when simulating it in larger supercells. All results reported in the main section of this paper are from 432-atom supercells.

Table II lists the atomic diffusion coefficients as extracted from the Einstein relation, $MSD(t) = 6 * D_{MSD} * t$, and from the velocity autocorrelation function, $D_{VACF} = \frac{1}{3} \int_0^\infty A_{vv}(t) dt$, where $A_{vv}(t) = \langle \vec{v}(t) \vec{v}(0) \rangle$. Changes in the
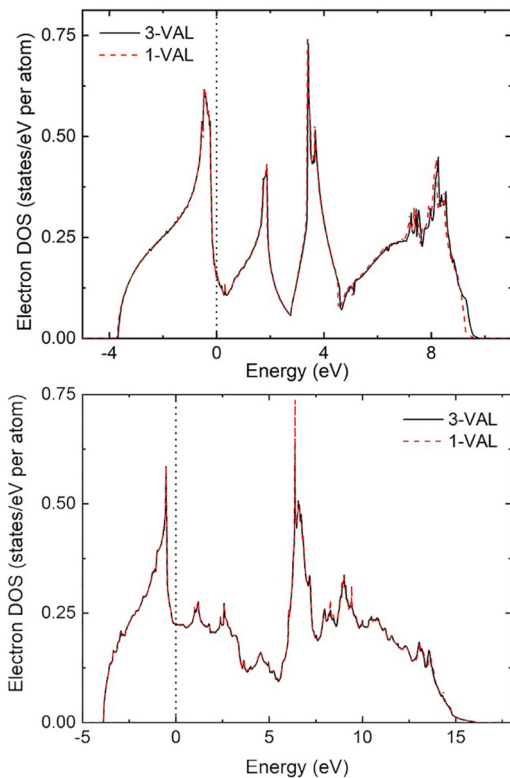

FIG. 11. Calculated electronic DOS of dense $cI16$ (top) and $C2/m$ (bottom) lithium at 50 GPa using both one- and all-electron PAW data sets.
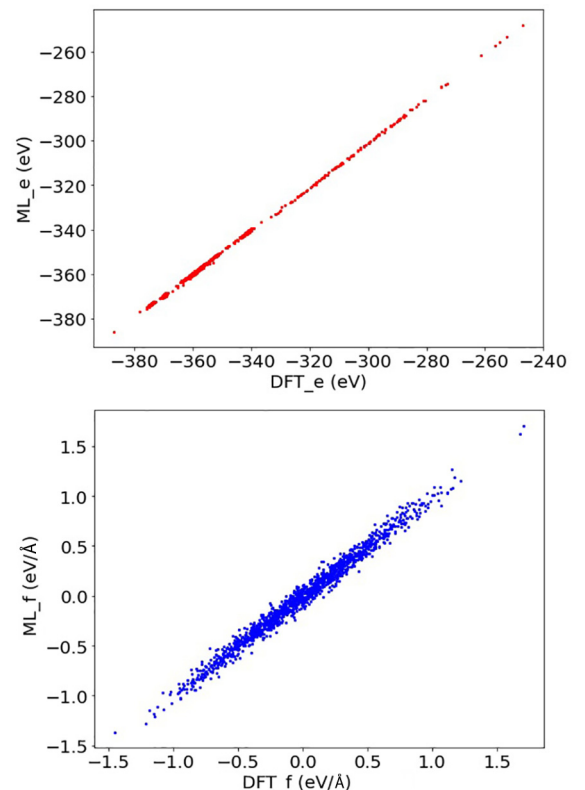

FIG. 12. Parity plots of total energies (E) and forces (F) for MD snapshots using the machine learning potential vs using DFT.
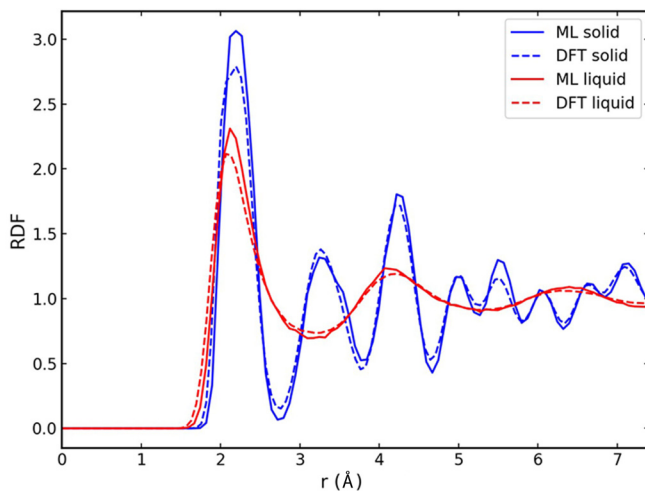
FIG. 13. Comparison of pair correlation function $g(r)$ of 160-K solid and 360-K liquid, computed with the MTP potential and AIMD.

order of magnitude of D distinguish different states and help determine the phase transition boundaries.

APPENDIX C: PSEUDOPOTENTIAL, MACHINE LEARNING TESTS

To test whether the Li one- and three-electron valence space PAW data sets are comparable, we calculated the valence electron DOS for both the $cI16$ and $C2/m$ structures; see Fig. 11. They agree very well, with only slight differences between them that confirm this choice does not change our conclusions in this pressure regime.

To ensure that the machine learned interatomic potential is suitable, we compared total energies and atomic forces for a series of snapshots against DFT values. The correlation is very good; see Fig. 12. Local structure, as captured by $g(r)$, also agrees very well, see Fig. 13, with the potential giving only very slightly overstructured results compared to DFT.

[1] J. B. Neaton and N. W. Ashcroft, Nature (London) **400**, 141 (1999).

[2] A. W. Overhauser, Phys. Rev. Lett. **53**, 64 (1984).

[3] S. F. Elatresh, W. Cai, N. W. Ashcroft, R. Hoffmann, S. Deemyad, and S. A. Bonev, Proc. Natl. Acad. Sci. USA **114**, 5389 (2017).

[4] G. J. Ackland, M. Dunuwille, M. Martinez-Canales, I. Loa, R. Zhang, S. Sinogeikin, W. Z. Cai, and S. Deemyad, Science **356**, 1254 (2017).

[5] B. Olinger and J. W. Shaner, Science **219**, 1071 (1983).

[6] M. Hanfland, I. Loa, K. Syassen, U. Schwarz, and K. Takemura, Solid State Commun. **112**, 123 (1999).

[7] M. Hanfland, K. Syassen, N. E. Christensen, and D. L. Novikov, Nature (London) **408**, 174 (2000).

[8] C. L. Guillaume, E. Gregoryanz, O. Degtyareva, M. I. McMahon, M. Hanfland, S. Evans, M. Guthrie, S. V. Sinogeikin, and H. K. Mao, Nat. Phys. **7**, 211 (2011).

[9] K. Shimizu, H. Ishikawa, D. Takao, T. Yagi, and K. Amaya, Nature (London) **419**, 597 (2002).

[10] V. V. Struzhkin, M. I. Eremets, W. Gan, H. K. Mao, and R. J. Hemley, Science **298**, 1213 (2002).

[11] S. Deemyad and J. S. Schilling, Phys. Rev. Lett. **91**, 167001 (2003).

[12] T. Matsuoka, M. Sakata, Y. Nakamoto, K. Takahama, K. Ichimaru, K. Mukai, K. Ohta, N. Hirao, Y. Ohishi, and K. Shimizu, Phys. Rev. B **89**, 144103 (2014).

[13] T. Matsuoka and K. Shimizu, Nature (London) **458**, 186 (2009).

[14] A. Lazicki, Y. Fei, and R. J. Hemley, Solid State Commun. **150**, 625 (2010).

[15] A. M. Schaeffer, W. B. Talmadge, S. R. Temple, and S. Deemyad, Phys. Rev. Lett. **109**, 185702 (2012).

[16] I. Tamblyn, J. Y. Raty, and S. A. Bonev, Phys. Rev. Lett. **101**, 075703 (2008).

[17] E. R. Hernandez, A. Rodriguez-Prieto, A. Bergara, and D. Alfe, Phys. Rev. Lett. **104**, 185701 (2010).

[18] M. Frost, J. B. Kim, E. E. McBride, J. R. Peterson, J. S. Smith, P. Sun, and S. H. Glenzer, Phys. Rev. Lett. **123**, 065701 (2019).

[19] B. Rousseau and N. W. Ashcroft, Phys. Rev. Lett. **101**, 046407 (2008).

[20] C. J. Pickard and R. J. Needs, Phys. Rev. Lett. **102**, 146401 (2009).

[21] Y. Yao, J. S. Tse, and D. D. Klug, Phys. Rev. Lett. **102**, 115503 (2009).

[22] M. Marques, M. I. McMahon, E. Gregoryanz, M. Hanfland, C. L. Guillaume, C. J. Pickard, G. J. Ackland, and R. J. Nelmes, Phys. Rev. Lett. **106**, 095502 (2011).

[23] J. Lv, Y. Wang, L. Zhu, and Y. Ma, Phys. Rev. Lett. **106**, 015503 (2011).

[24] Y. Feng, J. Chen, D. Alfe, X. Z. Li, and E. Wang, J. Chem. Phys. **142**, 064506 (2015).

[25] S. F. Elatresh, S. A. Bonev, E. Gregoryanz, and N. W. Ashcroft, Phys. Rev. B **94**, 104107 (2016).

[26] K. Xia, H. Gao, C. Liu, J. N. Yuan, J. Sun, H. T. Wang, and D. Y. Xing, Sci. Bull. **63**, 817 (2018).

[27] R. Martonak, A. Laio, and M. Parrinello, Phys. Rev. Lett. **90**, 075503 (2003).

[28] A. Laio and M. Parrinello, Proc. Natl. Acad. Sci. USA **99**, 12562 (2002).

[29] I. S. Novikov, K. Gubaev, E. V. Podryabinkin, and A. V. Shapeev, Mach. Learn. Sci. Technol. **2**, 025002 (2021).

[30] A. Carreras, A. Togo, and I. Tanaka, Comput. Phys. Commun. **221**, 221 (2017).

[31] V. Kapil, M. Rossi, O. Marsalek, R. Petraglia, Y. Litman, T. Spura, B. Q. Cheng, A. Cuzzocrea, R. H. Meissner, D. M. Wilkins *et al.*, Comput. Phys. Commun. **236**, 214 (2019).

[32] G. Kresse and J. Furthmüller, Comput. Mater. Sci. **6**, 15 (1996).

[33] P. E. Blochl, Phys. Rev. B **50**, 17953 (1994).

[34] J. P. Perdew, K. Burke, and M. Ernzerhof, Phys. Rev. Lett. **77**, 3865 (1996).

[35] S. Nose, J. Chem. Phys. **81**, 511 (1984).

[36] W. G. Hoover, Phys. Rev. A **31**, 1695 (1985).

[37] M. Parrinello and A. Rahman, Phys. Rev. Lett. **45**, 1196 (1980).

[38] G. S. Grest and K. Kremer, Phys. Rev. A **33**, 3628 (1986).

[39] S. Plimpton, J. Comput. Phys. **117**, 1 (1995).

[40] H. Gao, J. Wang, Y. Han, and J. Sun, Fundam. Res. **1**, 466 (2021).

[41] C. Liu, J. Shi, H. Gao, J. Wang, Y. Han, X. Lu, H. T. Wang, D. Xing, and J. Sun, Phys. Rev. Lett. **126**, 035701 (2021).

[42] C. Liu, H. Gao, Y. Wang, R. J. Needs, C. J. Pickard, J. Sun, H.-T. Wang, and D. Xing, Nat. Phys. **15**, 1065 (2019).

[43] C. Liu, H. Gao, A. Hermann, Y. Wang, M. Miao, C. J. Pickard, R. J. Needs, H.-T. Wang, D. Xing, and J. Sun, Phys. Rev. X **10**, 021007 (2020).

[44] H. Gao, C. Liu, A. Hermann, R. J. Needs, C. J. Pickard, H. T. Wang, D. Xing, and J. Sun, Natl. Sci. Rev. **7**, 1540 (2020).

[45] E. V. Podryabinkin, E. V. Tikhonov, A. V. Shapeev, and A. R. Oganov, Phys. Rev. B **99**, 064114 (2019).

[46] T. E. Markland and M. Ceriotti, Nat. Rev. Chem **2**, 0109 (2018).

[47] A. Togo and I. Tanaka, Scr. Mater. **108**, 1 (2015).

[48] E. Gregoryanz, L. F. Lundegaard, M. I. McMahon, C. Guillaume, R. J. Nelmes, and M. Mezouar, Science **320**, 1054 (2008).

[49] A. R. Oganov, R. Martonak, A. Laio, P. Raiteri, and M. Parrinello, Nature (London) **438**, 1142 (2005).

[50] J. Behler, R. Martonak, D. Donadio, and M. Parrinello, Phys. Rev. Lett. **100**, 185501 (2008).

[51] J. Sun, D. D. Klug, R. Martonak, J. A. Montoya, M.-S. Lee, S. Scandolo, and E. Tosatti, Proc. Natl. Acad. Sci. USA **106**, 6077 (2009).

[52] A. B. Belonoshko, T. Lukinov, J. Fu, J. J. Zhao, S. Davis, and S. I. Simak, Nat. Geosci. **10**, 312 (2017).

[53] H. X. Zong, V. N. Robinson, A. Hermann, L. Zhao, S. Scandolo, X. D. Ding, and G. J. Ackland, Nat. Phys. **17**, 955 (2021).

[54] C. J. Wu, P. Soderlind, J. N. Glosli, and J. E. Klepeis, Nat. Mater. **8**, 223 (2009).

[55] D. G. Sangiovanni, J. Klarbring, D. Smirnova, N. V. Skripnyak, D. Gambino, M. Mrovec, S. I. Simak, and I. A. Abrikosov, Phys. Rev. Lett. **123**, 105501 (2019).

[56] V. N. Robinson, H. X. Zong, G. J. Ackland, G. Woolman, and A. Hermann, Proc. Natl. Acad. Sci. USA **116**, 10297 (2019).

[57] Y. Wang, J. J. Wang, A. Hermann, C. Liu, H. Gao, E. Tosatti, H. T. Wang, D. Y. Xing, and J. Sun, Phys. Rev. X **11**, 011006 (2021).

[58] G. Woolman, V. N. Robinson, M. Marques, I. Loa, G. J. Ackland, and A. Hermann, Phys. Rev. Mater. **2**, 053604 (2018).

[59] T. Vicsek, A. Czirok, E. Ben-Jacob, I. I. Cohen, and O. Shochet, Phys. Rev. Lett. **75**, 1226 (1995).